Exp Fluids (2014) 55:1627
DOI 10.1007/s00348-013-1627-y

RESEARCH ARTICLE

An inexpensive and versatile technique for wide frequency range surface pressure measurements: an application for the study of turbulent buffeting of a square cylinder

Fernando Carbajo Fuertes · Enrico Cecchi · Jeroen van Beeck · Christophe Schram

Received: 6 May 2013 / Revised: 19 September 2013 / Accepted: 21 October 2013 / Published online: 28 November 2013

Abstract This work presents the development of an inexpensive measurement technique based on miniature microphones for the measurement of pressure fluctuations in a wide frequency range, starting from infrasound up to several kilohertz. Special emphasis has been put on achieving accurate calibration of the system at very low frequencies and good agreement with reference measurements have been achieved at frequencies as low as 1 Hz, therefore opening new low-budget research possibilities in many fields of fluid mechanics. The measurement technique proposed is specially indicated when the number of simultaneous pressure measurements is high since the sensors used are inexpensive, contrarily to common research equipment. One particular area in which this technique results useful is bluff-body aerodynamics. As an example of the potential of the technique, the structural response of a finite-square cylinder immersed in a turbulent flow is studied.

1 Introduction

Mapping unsteady surface pressures can become unfeasible from the point of view of cost of instrumentation if the number of simultaneous measurements is too high. Trying to resolve in time and space pressure fluctuations on a surface commonly involves the use of many expensive sensors, and their price increases significantly if a wide frequency range needs to be resolved.

This drawback can be overcome by using inexpensive microphones. The use of electret microphone cartridges for the measurement of unsteady surface pressures has several advantages: They have a high signal-to-noise ratio and a high sensitivity, they can be easily miniaturized and, most important of all, today's manufacturing technology easily allow their cost to be as low as two orders of magnitude smaller than other standard unsteady pressure sensors used in the laboratory. Kendall (1990) was one of the first to use flush-mounted electret microphones for the study of the boundary layer receptivity to free-stream turbulence.

The proposed measurement technique is inspired by Johnston and Sullivan (1994) in which a flush-mounted microphone is used for the measurement of low-amplitude unsteady pressure signals on an airfoil surface. During the projected wind tunnel experiments, these fluctuations can lead to saturation of the microphone signal at high velocities. In the present setup, a pressure line connects the surface pressure tap to the microphones. This has two main purposes. The first one is to reduce or damp the pressure fluctuations to acceptable limits. The second is to allow pressure measurement in configurations where there is not enough space to fit a microphone directly, therefore making the technique more versatile since using thin pressure lines is almost always possible.

The calibration of these sensors in frequency is one of the most important issues. It must be also possible to perform it in situ. Most of the previous experiments include modules for automatic calibration, and they require little or no compensation in terms of amplitude and phase and are

F. Carbajo Fuertes (✉) · E. Cecchi · J. van Beeck · C. Schram
Environmental and Applied Fluid Dynamics Department, von Karman Institute for Fluid Dynamics, Sint-Genesius-Rode, Belgium
e-mail: fernando.carbajo@epfl.ch

Present Address:
F. Carbajo Fuertes
Wind Engineering and Renewable Energy Laboratory, École Polytechnique Fédérale de Lausanne, Lausanne, Switzerland

limited to high-frequency ranges such as Lee and Sung (2002). The assessment of the frequency response of the chain composed by the tubing and the microphone itself is of paramount importance for the consistency of the measurements—see Sect. 2.2.2. Some authors have provided inspiration for the calibration method presented here such as Sullivan and Mueller (1999) or Lee and Sung (1999), both of them for polyvinylidene fluoride film sensors.

In many applications, it is important to accurately measure pressure fluctuations in a wide frequency range that include infrasound. Several methods for calibrating the response of microphones at infrasound frequencies are available, but the main requirement again is to be simple and inexpensive. Basten and de Bree (2010) presented a simple idea for the calibration at infrasound frequencies with a spherical speaker by introducing the microphones into it and sealing all the system. This idea inspired what is proposed here.

In the proposed measurement technique, the microphones are not flush-mounted on the surface but inside metal cylinders that are connected to the surface through pressure lines. The lines' length and diameter are expected to play an important role in the attenuation or amplification and delay of the pressure fluctuations depending on the frequency. The pioneering work of Bergh and Tijdeman (1965) and later Gumley (1983) must be a reference if this effect needs to be estimated in advance.

The proposed measurement technique has been applied in the field of bluff-body aerodynamics and turbulent buffeting of structures as an example of its potential. Specially relevant is the work of Surry et al. (1983) regarding simple measurements techniques for area pressure loads and Holmes (1990) for the analysis of pressure fluctuations on bluff bodies. Vickery (1990) described several experimental techniques for the determination of the dynamic response of structures immersed in turbulent flows. Finally, it cannot go unmentioned the extensive work of Surry and Djakovich (1995), Kareem and Cermak (1984), Kareem (1990) and Lee (1975) regarding fluctuating pressures on finite-square cylinders and also Davenport and Novak (2010) regarding aeroelastic response of structures in general.

2 Development of the technique

2.1 Principle of the technique

The main objective of the present work is to develop an inexpensive and versatile technique for the accurate measurement of unsteady pressures acting on surfaces for diverse applications. The principle of the proposed technique, sketched in Fig. 1, is very simple: A tap present on the exterior part of the model surface communicates the pressure through lines to a T-junction-like metal piece in which a miniature microphone is inserted. This microphone is responsible for the measurement of the pressure fluctuations. The other end of the T-junction is connected through another line to a scanning valve and then to a differential pressure transducer in order to measure the average pressure.

Special attention has to be paid for achieving a good sealing in all the system—especially for the insertion of the microphones inside the T-junction. Neglecting this issue would result in erroneous measurements of the average pressure as well as the low-frequency fluctuations.

The technique is cost-saving oriented. It is most effective when the number of simultaneous measurement points is high, e.g., space-resolved pressure acting on a bluff-body. Separating the pressure measurement into fluctuating and average components has an important advantage for statistically stationary processes: A single differential pressure transducer, with the help of a scanning valve, is sufficient to retrieve the average pressure at all points, while the fluctuations can be measured simultaneously by many miniature microphones. Suitable inexpensive transducers can be found easily in the market; in this case, *Knowles FG-23742-C05* electret microphones are used (40$ each approx).

2.2 Calibration

A correct static and dynamic calibration is fundamental when using this kind of systems since the microphones measure pressures different from those acting on the surface. The reasons for this are namely the attenuation effect of the tubing, possible resonances inside the T-junction or the pressure lines and the response of the microphones themselves. Low-cost microphones—like the ones used here—will most probably not have a certified flat response—contrarily to common research equipment—in a wide frequency range. On top of that, a big decay of the response is expected at low frequencies unless they are specifically designed (requirement normally incompatible with inexpensive equipment). This makes the calibration specially critical at infrasound frequencies.

The calibration process has several important requirements: It must be repeatable, accurate, and must allow in situ calibration and cover a wide frequency range starting from as low as possible. With the present equipment, pressure fluctuations are correctly measured at frequencies as low as 1 Hz.

2.2.1 Transfer functions concept

The reconstruction of the pressure at the surface is based on Fourier transforms $\mathcal{F}$ of periodic signals for the calculation of three different transfer functions. The transfer functions

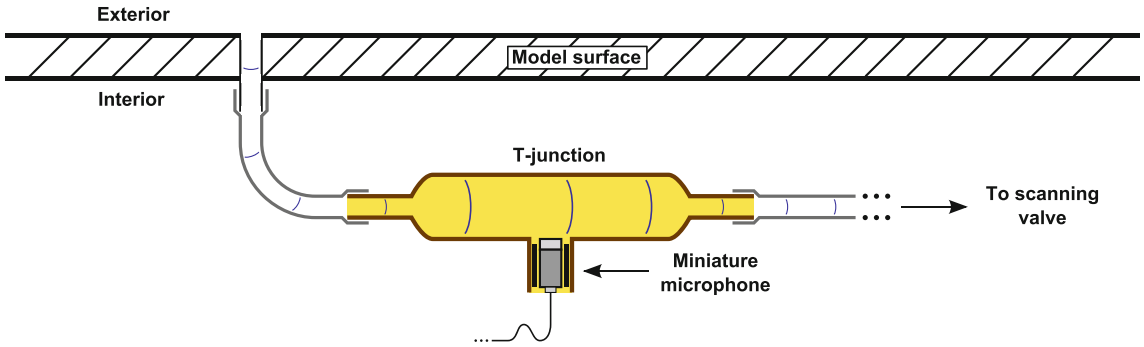

Fig. 1 Sketch of the designed system with the miniature microphone inserted in the cylindric junction

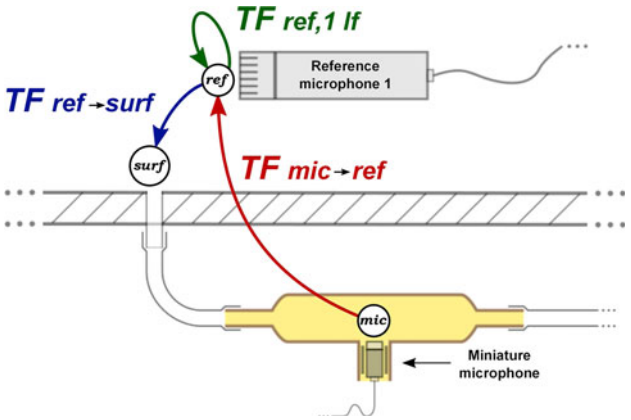

Fig. 2 Sketch of the reconstruction process in three steps

convert the original signal registered by the miniature microphone to the surface pressure that is felt where the tap is situated. This is done in three steps—applying the three transfer functions mentioned before—as sketched in Fig. 2 $TF_{mic\rightarrow ref}$ converts the original signal to that of a reference microphone placed at a known position outside the system. $TF_{ref\ lf}$ accounts for the response of the reference microphones at infrasound frequencies (this step can be skipped if infrasound microphones are used as references). $TF_{ref\rightarrow surf}$ is a purely spatial matter and it relates to the pressure at the point where the reference microphone is placed (inside the calibrator, see Fig. 2) and the pressure at the surface where the tap is placed.

2.2.2 Calculation of the transfer functions

The measuring equipment needed for the calculation of the transfer functions is very reduced: two high-quality microphones (from now on defined as 1 and 2) and a differential pressure transducer (DPT). The main element of the process is an ad hoc-designed calibration tube including a 2″, 8Ω, 60 W speaker able to generate pressure fluctuations when fed by a signal generator. The tube has a hole in its side in which a reference microphone (in this case a B&K 4191 $\frac{1}{2}''$ free-field microphone) is flush-mounted. One end is open for direct contact with any flat surface. The configuration of the previous elements is different for each transfer function, and it is detailed below.

The following steps are followed in order to get all the transfer functions (see Fig. 2):

1. Static calibration of the two reference microphones—β_{ref}
2. Estimation of the transfer function for the infrasound response of the reference microphones—$TF_{ref\ lf}$
3. Estimation of the transfer functions between the miniature microphones output inside the T-junction and a reference microphone flush-mounted on the calibration tube—$TF_{mic\rightarrow ref}$
4. Estimation of the transfer function between the reference microphone position and the pressure tap at the wall surface—$TF_{ref\rightarrow surf}$

Reference microphones static calibration The static calibration of the reference microphones is done with a pistonphone calibrator which produces a sinusoidal pressure fluctuation at a known frequency and sound pressure level p_{rms}. The output of the microphone is a voltage that is evaluated in terms of voltage fluctuations V_{rms}; the calibration factor β_{ref} is defined as follows:

$$\beta_{ref\ 1,2} = \frac{p_{rms}}{V_{rms_{1,2}}} \quad (1)$$

which directly converts voltage to pressure for the range of frequencies specified by the manufacturer.

Reference microphones correction for infrasound frequencies If the reference microphones are not specially suited for infrasound measurements, then their response to low-frequency pressure fluctuations must be correctly characterized. This is done with the help of a common differential pressure transducer (in this case, Validyne DP15). One end is open to ambient pressure through a very long thin pressure line for damping of possible pressure ambient fluctuations, and the other is connected to the calibrator pressure through a short pressure line; the latter

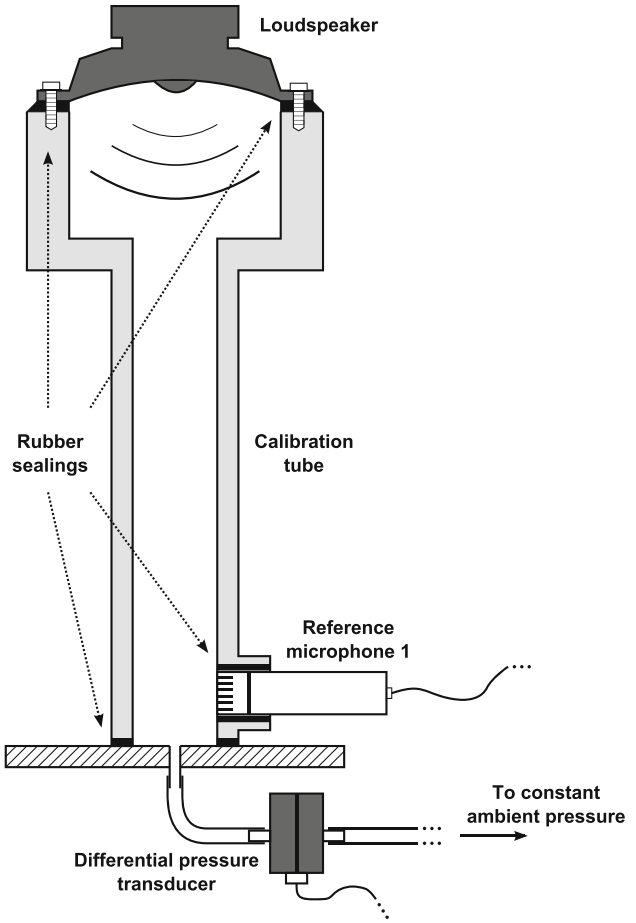

Fig. 3 Disposition of the elements for the estimation of the infrasound response of the reference microphones, see Fig. 2

is as short as possible so that its response is constant up to frequencies higher than 20 Hz, thus creating an overlapping frequency range where the response of the DPT and the reference microphone is flat.

Figure 3 shows the calibration tube and the disposition of the elements: the loudspeaker on top, the reference microphone 1 flush-mounted on the side and the DPT connected to the surface pressure tap. Given the size and quality of the speaker, it is not possible to generate low-frequency pressure levels higher than the ordinary background noise in a common room. This problem is solved by achieving a tight sealing of the tube by using rubber joints in all contact zones between elements to prevent any leaking. Like this, the membrane of the speaker effectively acts as a moving piston and the pressure levels achieved inside the calibration tube are rather constant up to its first resonance frequency. This solution was inspired by Basten and de Bree (2010).

The speaker is fed geometrical or exponential chirp functions covering wide frequency ranges. A simple

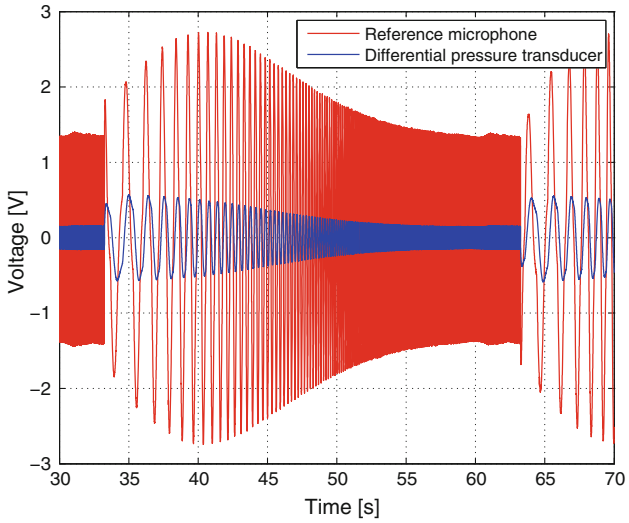

Fig. 4 Example of the registered signals, see Fig. 3

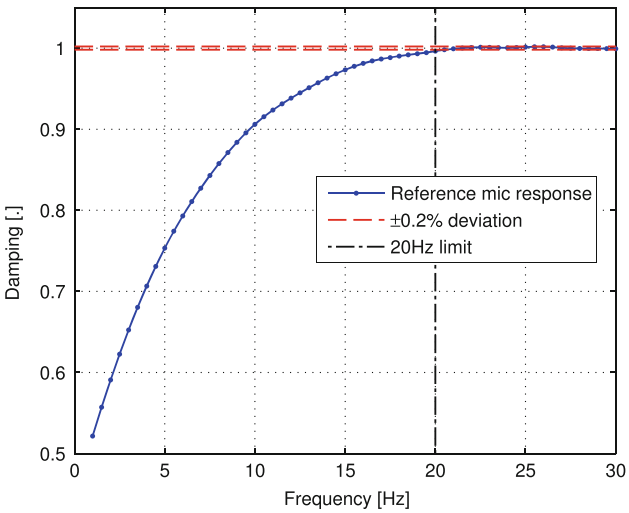

Fig. 5 Example of the transfer function $TF_{ref\ 1,2\ lf}$

analysis of the registered signals (example in Fig. 4) allows the calculation of the transfer function needed.

The transfer function for each of the reference microphones 1 and 2—is calculated as follows:

$$TF_{ref\ 1,2\ lf} = C_{norm} \frac{\left|\mathcal{F}\left(V_{ref\ 1,2}(t)\right)\right|}{\left|\mathcal{F}(V_{DPT}(t))\right|} \quad (2)$$

An example is shown in Fig. 5. The transfer function is presented averaged in blocks of 0.5 Hz from 1 to 20 Hz. It is also normalized using the average value of itself in the frequency range 21–35 Hz, (C_{norm}) where it is flat (within a 0.2 ± % variation). Even though the microphones used are not designed for infrasound measurements, their output is still higher than 50 % of the reference value at a frequency as low as 1 Hz. Then, using $TF_{ref\ 1,2\ lf}$ all measurements can be easily corrected in the range 1–20 Hz.

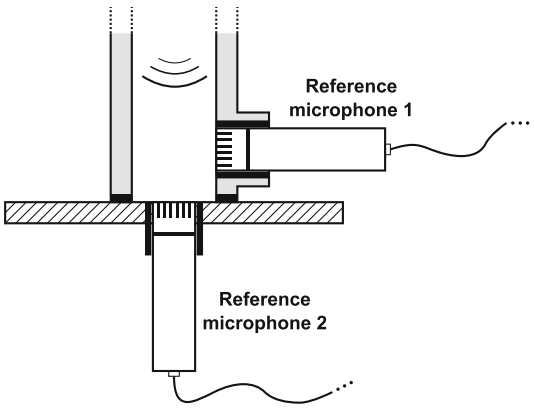

Fig. 6 $TF_{ref\rightarrow surf}$ setup detail, see Fig. 2

Reference microphone to surface-mounted microphone The second transfer function to be applied is a purely spatial matter, and it is needed for allowing in situ calibration of the microphones. It transforms the pressure at the side of the calibrator tube to the one at the surface where the pressure tap is located. This is achieved using both reference microphones as shown in Fig. 6.

The transfer function is calculated as follows:

$$TF_{ref\rightarrow surf} = \frac{\mathcal{F}\left(\beta_{ref,1}\cdot V_{ref,1}(t)\right)\cdot\left(1/TF_{ref,1\,lf}\right)}{\mathcal{F}\left(\beta_{ref,2}\cdot V_{ref,2}(t)\right)\cdot\left(1/TF_{ref,2\,lf}\right)} \quad (3)$$

where the subindexes $_{1,2}$ are used to denote the reference microphones in the calibrator tube and in the location of the pressure tap, respectively.

This transfer function has to be calculated only once for each calibration tube since what are being compared are true corrected pressures measured at two different points and not unprocessed voltage signals like in the rest of the cases. An example of $TF_{ref\rightarrow surf}$ is shown in Fig. 7. At low frequencies, the pressure at the side of the calibration tube and at the surface are the same and are felt practically at the same time (modulus one and phase zero). This does not hold true when approaching the first longitudinal resonance frequency of the calibration tube (at around 2.5 kHz).

The rest of the resonance frequencies (longitudinal and transversal) happen at higher frequencies than 5 kHz that has been arbitrarily considered the effective upper limit frequency for the present system (once the amplitude of the signal has decayed to 30 %). This limit can be pushed higher by using calibration tubes with different lengths and diameters. The practical high-frequency limit of the system depends on the length and diameter of the line that connects the pressure tap with the T-junction since it is the responsible for the damping of the high-frequency pressure fluctuations.

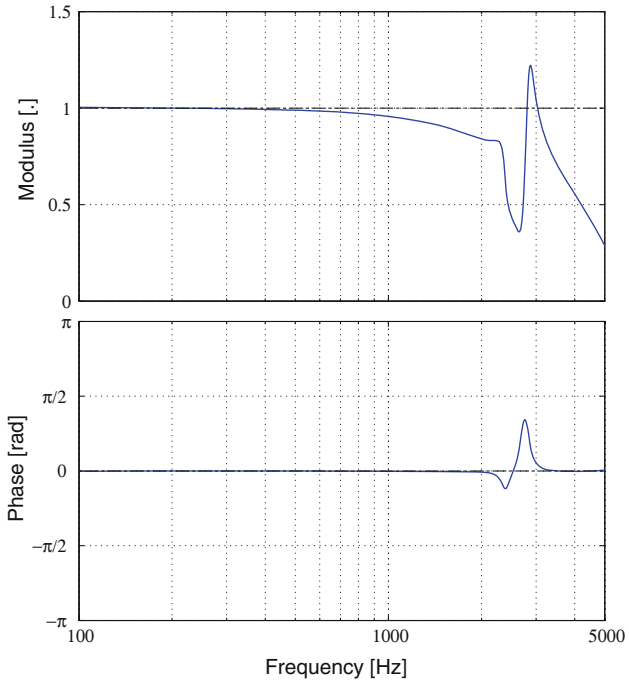

Fig. 7 $TF_{ref\rightarrow surf}$ modulus and phase, see Fig. 6

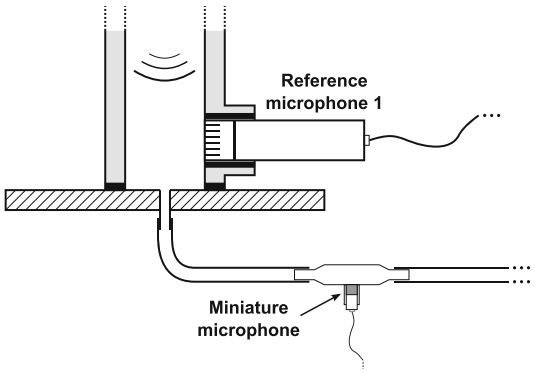

Fig. 8 $TF_{mic\rightarrow ref}$ setup detail, see Fig. 2

Miniature microphone to reference microphone The third transfer function converts the signal that is measured by the miniature microphone inside the T-junction to the one measured by the reference microphone flush-mounted on the interior surface of the calibration tube. The configuration of the different elements for the calibration is shown on Fig. 8 in which each of the miniature microphone is inserted into a T-junction, and it is already connected to the same line that will be used during the experiments.

The transfer function is calculated as follows:

$$TF_{mic\rightarrow ref} = \frac{\mathcal{F}(V_{mic}(t))}{\mathcal{F}\left(V_{ref,1}(t)\right)} \quad (4)$$

2.2.3 Reconstruction of the unsteady surface pressure

Once all the transfer functions are calculated, the reconstruction of pressure fluctuations at the exterior surface of the wall $P_{\text{surf}}(t)$ from the voltage measured by the miniature microphone output $V_{\text{mic}}(t)$ is reconstructed as follows (recall Fig. 2):

$$\text{TF}_{\text{mic}\to\text{surf}} = \text{TF}_{\text{mic}\to\text{ref}} \cdot \text{TF}_{\text{ref,1 lf}} \cdot \text{TF}_{\text{ref}\to\text{surf}} \tag{5}$$

$$P_{\text{surf}}(t) = \beta_{\text{ref,1}} \cdot \mathcal{F}^{-1}\left(\frac{\mathcal{F}(V_{\text{mic}}(t))}{\text{TF}_{\text{mic}\to\text{surf}}}\right) \tag{6}$$

where the transfer functions effectively convert in three steps the microphone signal to pressure at the surface of the wall as sketched on Fig. 2 and using the β_{ref} coefficient, which is needed to finally convert voltage to pressure.

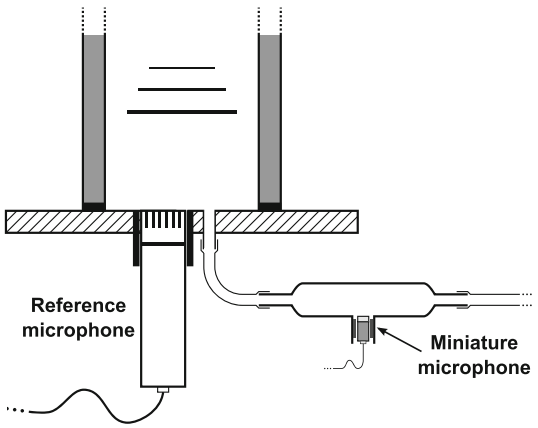

Fig. 9 Disposition of the elements for the validation test

2.3 Validation

The final phase of the development of any measurement technique is a validation campaign. The main idea behind the validation experiment is to be able to generate and measure accurately a reference fluctuating pressure at the same time and at the same exact position of the pressure tap. Evidently, the same-location requirement is impossible to fulfill, so a work-around solution has been developed: The calibration tube is placed on a wall in which a reference microphone has been flush-mounted and next to it, and as close as possible, a surface pressure tap connected to the proposed system, as shown in Fig. 9. This ensures that the speaker will produce planar pressure waves if their frequency is below the first transversal resonant mode of the tube.

The test is therefore simple: The speaker is fed with a large combination of sinusoidal signals with random amplitudes and frequencies; then, the signals of the reference and the miniature microphone are registered; an example is shown in Fig. 10 left.

Then, the reference microphone signal is corrected for low frequencies using the transfer function $\text{TF}_{\text{ref lf}}$ as calculated in Eq. 2, yielding the effective reference pressure. The miniature microphone signal is reconstructed using $\text{TF}_{\text{mic}\to\text{surf}}$, from Eq. 6 (see Fig. 10 right). In all cases studied, the standard deviation of the difference between reference and reconstructed pressures has always been less than 6.1 % of the standard deviation of the reference pressure. Similarly, the differences between reference and reconstructed maxima were always below 8.4 %.

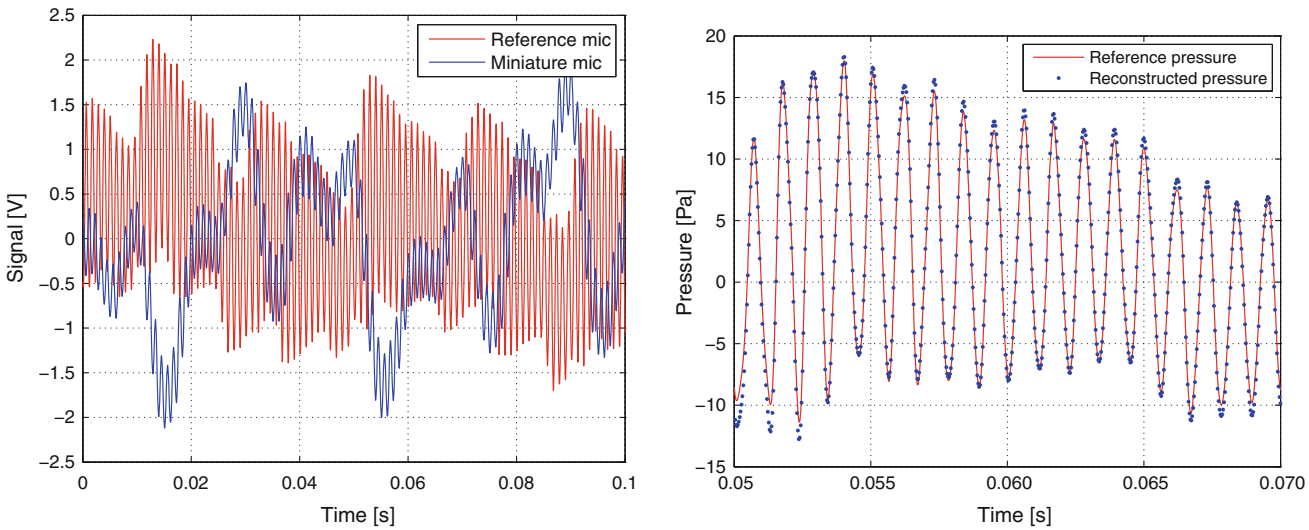

Fig. 10 *Left* example of the microphone signals for one validation test, see Fig. 9. *Right* detail of the reference and reconstructed pressure signals

3 Turbulent buffeting of a square cylinder

As stated previously, this technique has a wide range of applications. A particularly suitable one, which is presented here, is bluff-body aerodynamics. The example investigated regards the structural response of a finite-square cylinder immersed in a turbulent flow.

The study is based on a blind comparison between a fully elastic model test and the method of integrated pressure forces on a rigid model proposed by Vickery (1990). The latter is a very powerful tool for the analysis of pressure forces surfaces and structural response of bluff bodies despite its simplicity. Its concept is easy to understand if one thinks in terms of the equation of motion,

$$F(t) = M\ddot{x}(t) + C\dot{x}(t) + Kx(t) \tag{7}$$

where x is the displacement—or rotation—vector of all the degrees of freedom of the structure, $\dot{x}$ and $\ddot{x}$ its time derivatives, $F(t)$ the force—and torque—vector applied, respectively, on each of them. M and K are, respectively, the mass and stiffness matrices and C is the damping matrix, which can be approximated using the mass and stiffness matrices though the Rayleigh damping parameters α and β:

$$C = \alpha M + \beta K \tag{8}$$

Equation 7 can be easily solved using the assumption that the forces $F(t)$ are not dependent on the deformations of the structure or its movement—independent of $x, \dot{x}$ and $\ddot{x}$—or in other words, the forces and the response are *uncoupled*. If this assumption is valid, the pressure forces can be measured on a *rigid model* and then used as inputs for a dynamic FEM analysis of the structure. The results of an experiment in which the displacements of an elastic model are measured and another in which the displacements are estimated using pressure measurements on a rigid model can be compared. Being two independent random (turbulent) processes, the statistical ensemble of both results must be the same.

The main disadvantage of this method is that it is unable to account for aeroelastic coupled phenomena such as vortex shedding lock-in, galloping, etc. On the other hand, in many cases, the possibility of undergoing these phenomena can be assessed in advance by hand calculations or experience.

The steps of the present study are the following (see work-flow sketch in Fig. 11):

0. Two independent experiments are carried out under the same inflow conditions (elastic and rigid models)

A. Rigid model approach

- A1. The unsteady pressure is measured directly on the surface of the *rigid model* using the technique presented in the previous section.
- A2. A FEM model of the *elastic cylinder* is built, including the elastic properties, damping, and mass distribution.
- A3. A dynamic FEM analysis is performed in which the forces acting on the structure are the ones measured on the rigid model in the wind tunnel, correctly scaled if necessary. The stresses and deformations of the structure can be calculated by means of a dynamic FEM analysis of the problem.
- A4. The *calculated displacements* of the top section of the FEM model are analyzed.

B. Fully elastic test

- B1. The horizontal displacement of the top section of the elastic cylinder is measured from above by means of high-speed imaging.

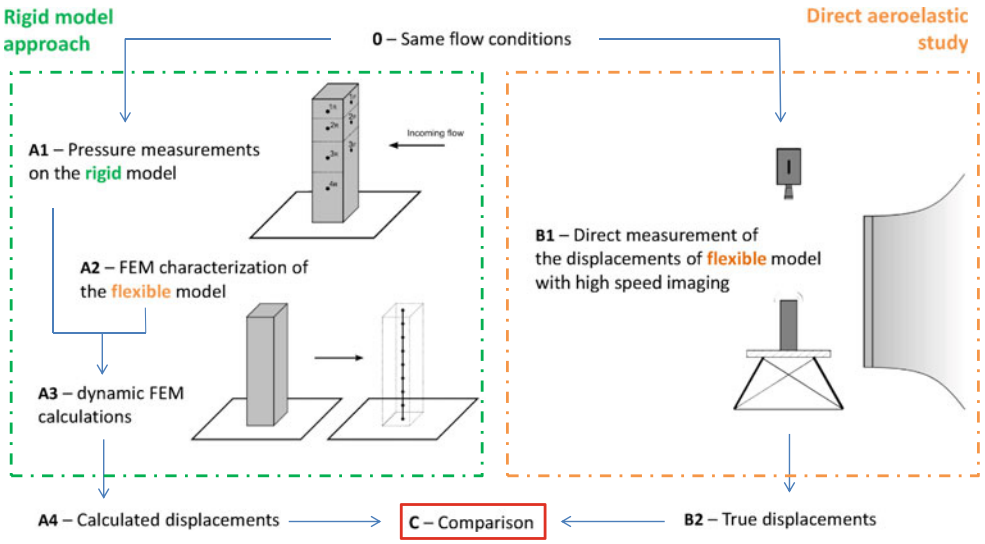

Fig. 11 Sketch of the present study. It is a blind comparison between the study of the elastic model and the rigid model approach combined with the measurement technique proposed in Sect. 2

B2. The *measured displacements* of the top section of the elastic cylinder are analyzed.

C. The results of the true displacements and the calculated ones are compared.

3.1 L1 wind tunnel

All the experiments presented from here on have been carried out in the open test section of the L1 wind tunnel at *VKI*. It consists of a round free-jet test section of 3 m diameter and 4.5 m length. The contraction ratio is 4:1 with a typical turbulence level at the outlet of 0.3 %.

The models used are placed on a horizontal platform that is situated 0.5 m higher than the bottom part of the jet (see Fig. 12).

3.2 Cylinder models and instrumentation

The test regards the study of the response of a finite-square cylinder of ratio 4:1 with dimensions 400 × 100 × 100 mm. As explained above, two models are needed: a *flexible* one, whose structural characteristics have to be determined (and modeled), and a *rigid* one (in order to avoid any displacement) for the measurement of the pressure on its surface.

The desired structural boundary condition for the flexible model is a *clamping* at its base. This ideal condition is approximated in practice by an ad hoc-designed and built support structure in four pieces. It prevents displacements and rotations at the base level by exerting a high but gently distributed pressure on the model walls below the platform without deforming it appreciably. This structure is in practice used to hold both the flexible and the rigid models.

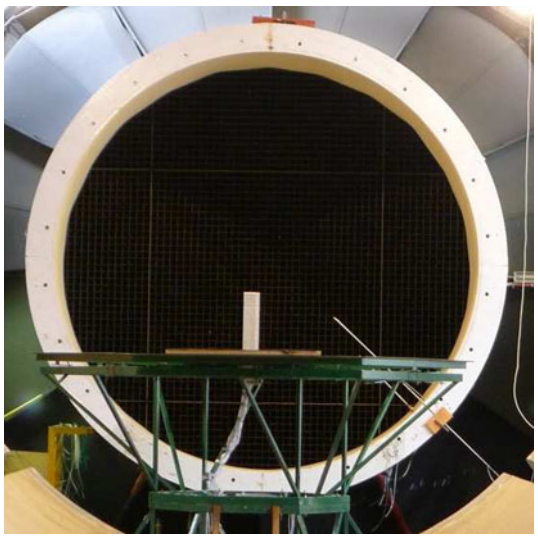

Fig. 12 Support platform and model in front of the *VKI* L1 wind tunnel contraction

The dimensions of both models when exposed to the flow are 400 × 100 × 100 mm. Both of them are actually longer (200 mm more) in order to allow the support to hold them correctly. The flexible model is made of a solid piece of polystyrene foam. The rigid model is made of aluminum plates of 0.6 mm thickness assembled together, therefore ensuring a much higher stiffness than the flexible model.

The displacements of the flexible model are measured by means of a high-speed camera (*Vision Research "Phantom" v7.1 CMOS*) that is installed above the building model and outside of the jet flow to avoid any vibration. The camera is used together with a *Nikkor* 200 mm *f*/4 objective because of the relatively big distance between the top of the model and the camera (2.5 m approx.). Its outputs are multi-tiff grayscale image files with a maximum resolution of 800 × 600 pixels. A target containing a big number of black circles or dots is attached to the top section of the model. The tracking of the displacements is done by identifying all the centers of the dots using a Matlab algorithm based on Hough transformations for shape detection. The particular parameterization for the circle detection used here (rho-theta) was first described by Duda and Hart (1972). The precision achieved with the current system and algorithm for relative displacements bigger than 0.1 mm is between 0.2 and 0.9 %.

The displacements of the rigid model are also evaluated using the same technique, and they are found to be always at least two orders of magnitude smaller than those of the flexible one. This fulfills the condition of rigidity of the model, necessary for a correct measurement of the pressure on its walls.

The rigid model has 4 surface pressure taps along the vertical center line of each lateral wall and 3 in the front and back walls. They are situated at different heights reported in Table 1 measured from the bottom of the model, see Fig. 13. The total number is 14 simultaneous pressure measurements, number limited by the amount of miniature microphones and channels available for this study. The taps are holes of 1 mm diameter, drilled perpendicularly to the model surface.

Table 1 Nomenclature of the different measurement points on the different model surfaces

Height	Model surface			
	Front	Back	Right	Left
H1 = 360 mm	1F	1B	1R	1L
H2 = 310 mm	2F	2B	2R	2L
H3 = 190 mm	3F	3B	3R	3L
H4 = 70 mm	-	-	4R	4L

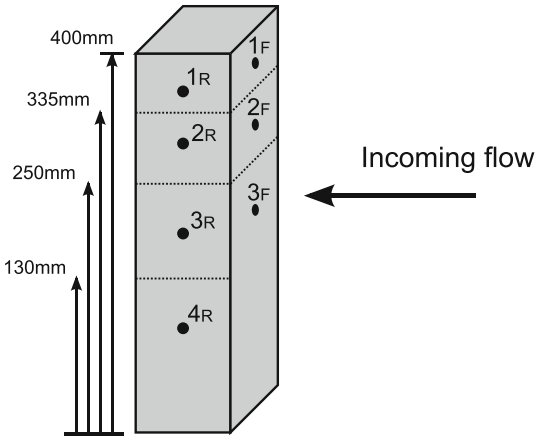

Fig. 13 Discretization of the pressure on the rigid model walls

3.3 Structural calculations

The pressure forces have to be discretized to be used as inputs for the dynamic FEM analysis. Being this discretization limited to 14 measurement points, it becomes extremely coarse and therefore the biggest source of error of the whole process. Figure 13 presents the areas in which the measured pressures have been arbitrarily considered as constant. Vickery (1990) suggests that for a correct characterization of the pressure acting on structures like the one studied here, the number of simultaneous pressure measurements is likely to be of the order of 100 per side.

Once the pressure fluctuations are measured on the model walls by means of the measurement technique developed and detailed previously, the structural response of the cylinder can be calculated by solving Eq. 7. In this case, it is simply done by using an explicit time integration method. The analysis is performed using a central differences method, and the behavior of the structures is assumed to be linear for small deformations.

The flexible model can be structurally defined as a vertical *cantilever beam* of constant square section and aspect ratio 4:1 with dimensions of 400 × 100 × 100 mm. This structure is discretized into 20 one-dimensional *beam elements* using Abaqus software (B31 Timoshenko elements, see Dassault's Abaqus theory manual). The boundary condition is therefore simple to model: The structure is *clamped* at its base, so all displacements and rotations of the node in contact with the ground are constrained.

The structural characteristics of the flexible model are determined experimentally, see Table 2. The motion of the top section is studied in several free-vibration tests with the help of the high-speed camera for an estimation of the logarithmic decrement δ, which is defined as follows:

Table 2 Measured characteristics of the elastic structure

Density (ρ)	78.30 kg/m^3
Young's modulus (E)	18.08 MPa
Logarithmic decrement (δ)	0.1075
First eigenfrequency	46.5 Hz

$$\delta = \ln \frac{A_n}{A_{n+1}} \tag{9}$$

where A_n and A_{n+1} are the amplitudes of two consecutive oscillations. Then, the logarithmic decrement is related to the *damping factor* or *damping ratio* ξ through the following formula:

$$\xi = \frac{\delta}{\sqrt{(2\pi)^2 + \delta^2}} \tag{10}$$

The average decrement between consecutive peaks is $A_n/A_{n+1} = 1.1135$. This yields a logarithmic decrement of $\delta = 0.1075$ and a damping ratio of $\xi = 20.20 \times 10^{-3}$.

The damping ratio can be related to the Rayleigh parameters α and β through Rayleigh's equation:

$$\xi = \frac{1}{2}\left(\frac{\alpha}{\omega} + \beta\omega\right) \tag{11}$$

One last arbitrary decision has to be taken since there are two unknowns and there is only Eq. 11 available. It is common practice to fix values of α several orders of magnitude bigger than β. A fixed value of $\alpha = 0.15$ is used.[1] Since the eigenfrequency is 46.5 Hz, this determines then a value of $\beta = 1.3652 \times 10^{-4}$.

Once the FEM model of the structure is complete, a simple test case is studied in order to check its validity. The motion of the beam model when subjected to the same instantaneous sudden unloading (and free-vibration) as used on the experiments is computed using the same explicit analysis method that the one used for the rest of the study. The good agreement between experimental data and the results from the dynamic FEM simulation can be considered as a proof that the FEM model built can actually characterize correctly the structural dynamics of the flexible model, therefore validating it for the rest of the calculations.

4 Results and discussion

In this section, only some of the most significant results of the study are presented. They regard mainly some general

[1] Values of α of different orders of magnitude were tried as well, but no significant difference on the calculations arose. Therefore, an arbitrary value of 0.15 was fixed and used thereafter.

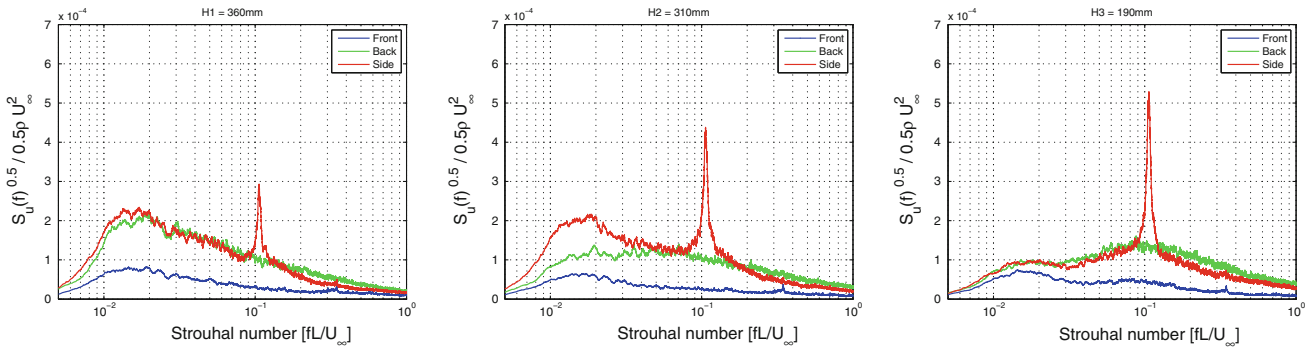

Fig. 14 Example of pressure spectra at different heights. $U_\infty = 24.8$ m/s, $Re = 169,000$

characteristics of the unsteady pressure measurements on the model walls and the measured and FEM-calculated displacement at its top section.

The pressure is adimensionalized with the dynamic pressure calculated from the velocity measured at the end of the contraction of the wind tunnel U_∞; the displacements of the top section are adimensionalized with the model height L (400 mm). The frequency in the spectra plots is expressed in terms of the Strouhal number:

$$St = \frac{fB}{U_\infty} \tag{12}$$

where B is the width of the square cross section of the model (100 mm). Results are also expressed in terms of the following definition of the Reynolds number:

$$Re = \frac{U_\infty B}{v} \tag{13}$$

4.1 Surface pressure

4.1.1 Surface pressure spectra

The spectra of the unsteady pressure acting at different points of the rigid model walls are presented here. Figure 14 shows the typical pressure spectra at the front, back, and side walls of the cylinder at three different heights.

The most relevant fact is the clearly defined peak that appears when studying the pressure fluctuations at the side walls (red color). This is the effect of the vortex shedding around the cylinder. The vortex shedding appears always at the same Strouhal number, 0.108, which agrees with the one expressed by Kareem (1990), Kareem and Cermak (1984) for finite-square cylinders of the same aspect ratio although immersed in simulated boundary layers and not in homogeneous flow.

The spectra of the pressure on the front and back walls do not show any peaks. Spectra on the sides and back walls at the same heights are similar—except for the absence of the peak at the shedding frequency—whereas the spectra on the front face are much lower. According to other experiments (Lee 1975), pressure fluctuations on the front surface mainly depend on the turbulence of the incoming flow which is low in this case, see Sect. 3.1. Closer to the top of the model—H1—the spectra have very important components at low frequencies, whereas close to the bottom—H3—they are shifted to higher frequencies, around the vortex shedding frequency. The periodic fluctuations on the sides are less defined (lower peak on the spectrum) when closer to the free end of the model. This agrees with Lee (1975), Surry and Djakovich (1995).

4.1.2 Surface pressure correlation

The pressure correlation matrices give an idea of how correlated are the loads at different points of the model. This has a direct impact on the body response in qualitative and also quantitative terms. The correlation term expressed here between two elements i, j is calculated as follows:

$$R(i,j) = \frac{C(i,j)}{\sqrt{C(i,i)C(j,j)}} \tag{14}$$

being $C(i, j)$ the covariance of the pressure fluctuations calculated as follows:

$$C(i,j) = E[P_i'(t) \cdot P_j'(t)] \tag{15}$$

where $P'(t)$ denotes the fluctuating or unsteady pressure defined as $P'(t) = P(t) - \overline{P}$.

Table 3 shows a typical correlation matrix that has been divided into four zones representing the four walls of the model. The color code for a simpler visualization and understanding of these correlations is the following: All the terms that show low correlation $-0.1 < C(i, j) < 0.1$ are dulled in gray. Gray background means negative correlation $C(i, j) < -0.1$, and black background means high correlation $C(i, j) > 0.1$ between pressures measured on the same wall.

The first fact to be noticed is that the correlations among the pressures measured at the back wall are close to zero, contrarily to what happens on the rest of the walls, where

Table 3 Example of pressure correlation matrix

		Front			Back			Left				Right			
		H1	H2	H3	H1	H2	H3	H1	H2	H3	H4	H1	H2	H3	H4
Front	H1	1.00													
	H2	0.61	1.00												
	H3	0.39	0.53	1.00											
Back	H1	0.27	0.20	0.07	1.00										
	H2	0.15	0.12	0.04	0.18	1.00									
	H3	0.01	0.02	0.01	0.01	0.01	1.00								
Left	H1	0.01	0.07	0.10	-0.02	0.01	0.02	1.00							
	H2	0.02	0.04	0.05	0.02	0.02	0.02	0.79	1.00						
	H3	0.00	-0.01	-0.02	0.02	0.01	0.00	0.30	0.48	1.00					
	H4	0.01	0.00	-0.04	0.04	0.03	0.01	0.13	0.28	0.57	1.00				
Right	H1	0.00	0.07	0.10	-0.05	-0.01	-0.01	0.19	-0.01	-0.24	-0.26	1.00			
	H2	0.02	0.06	0.05	0.01	0.00	-0.01	0.00	-0.15	-0.33	-0.34	0.75	1.00		
	H3	0.00	0.00	-0.01	0.00	-0.02	-0.02	-0.23	-0.32	-0.46	-0.48	0.23	0.40	1.00	
	H4	0.01	0.00	0.00	0.01	0.01	-0.01	-0.27	-0.36	-0.50	-0.47	0.11	0.25	0.56	1.00

U_∞ = 17.2 m/s, Re = 117,000

these correlations are always positive—black background. The high correlations on the front wall are caused by the fact that the pressures fluctuations depend mainly on the incoming flow (Lee 1975) . The low correlation at the back wall is explained by the flow topology of the recirculating zone, in which the coherent structures are smaller and probably do not influence two points at the same time. According to theory, the correlation increases with the characteristic size of the coherent structures at those points and decreases with their distance. The correlation matrices presented here agree generally with this fact.

The high positive correlations among the pressures at the side walls are a result of the vortex shedding. This fact is further confirmed by the negative correlations between points at opposite side faces—when on the left side, there is positive pressure, on the right one, there is negative pressure and vice versa—caused by a phase of 180 degrees between both sides.

The characteristic negative correlation between points on opposite sides due to the vortex shedding vanishes with height by the effect of the free end of the cylinder. It can be seen that the negative correlation is reduced to −0.15 at H2, and it even becomes positive 0.19 at H1.

It can also be noticed that the closer two points are, the higher the correlation we find—in absolute terms, positive or negative. This is a rather obvious observation, and it can be noticed by the fact that the main diagonals of the different sub-matrices contain the higher correlation values—positive and negative—whereas the other ones contain generally lower values.

These correlation matrices shown here are a consequence of the flow topology, influenced by the incoming turbulence, the vortex shedding, the recirculation region, and the aspect ratio of the model. The results presented here are in agreement with Holmes (1990), Lee (1975).

The discussion on the correlation between two adjacent pressure measurements in the same face of the model is of utmost importance when it comes to the decision about the discretization of the areas in which the pressure is considered constant. The higher the correlation, the better the assumption of the constant pressure over a defined area. Following this reasoning, better results are expected for the transversal calculations of the motion of the cylinder than for the longitudinal one due to the very low correlation between measurements shown at the back surface.

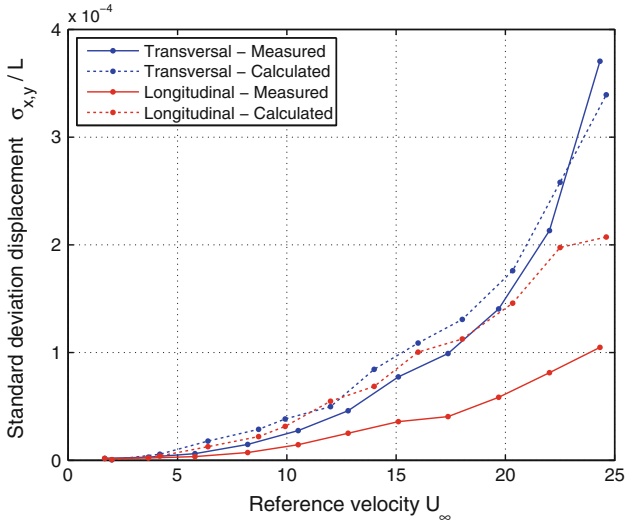

Fig. 15 Measured and calculated displacements of the top section. $15{,}000 \leq Re \leq 169{,}000$. See Fig. 11

4.2 Measured and calculated displacements

The high-speed camera has obtained images of the target attached to the top section of the flexible model at a rate of 500 Hz for duration of 18 s, the latter limited by the buffer memory of the camera. The result of the dynamic FEM simulations is evaluated for a similar time length. The first two seconds of each simulation are discarded in order to avoid any residual effect of the initial conditions—undeformed still beam—being this time much longer than that associated with the first eigenfrequency −46.5 Hz.

4.2.1 Standard deviation

The longitudinal and transversal standard deviation of the displacements of the top section, σ_x and σ_y, respectively, at difference reference velocities are presented in Fig. 15. This corresponds to the blind comparison exercise sketched in Fig. 11.

The transversal displacements measured are significantly higher—from two to three times bigger—than the longitudinal ones for the whole regime of velocities studied. Taking into account the serious limitations of the setup—only 14 simultaneous measurements—there is a relatively good agreement between the measured and calculated transversal displacements; the relative differences decrease from 30 % at 10 m/s to 10 % at 25 m/s.

On the other hand, the comparison for the longitudinal displacements shows a rather big quantitative disagreement. The calculated displacements are systematically found to be around two times bigger than those measured on the flexible model. This can be explained through the surface pressure correlation matrix—Sect. 4.1.2—and the discretization of the surface pressures—Fig. 13. For the FEM calculations, it is assumed that the pressure measured at each point—Table 1—is constant in all the area detailed; the lower the correlation between two adjacent points, the bigger the error of this approximation. It is specially critical for the back side of the model. Let us consider the positions 2B and 3B as an example: The correlation between these two pressures is practically zero ($C = 0.01$); nevertheless, the pressure on each area is considered as perfectly correlated ($C = 1$) to each one inside their respective area. This is far from being true and therefore results in higher calculated forces acting on the model, and therefore higher displacements.

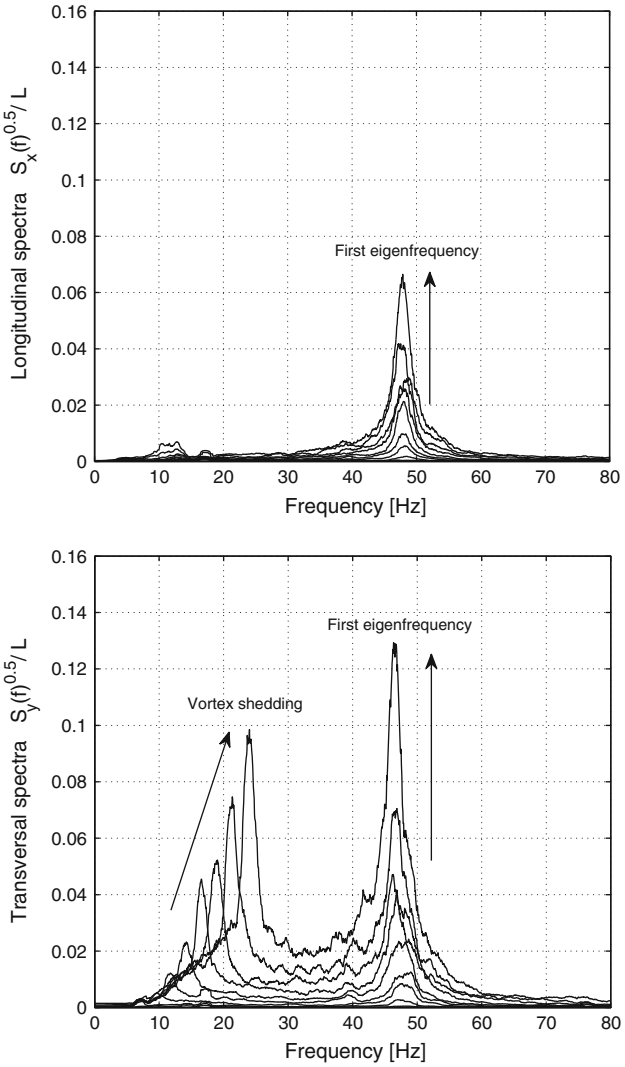

Fig. 16 Evolution of measured spectra of the response with increasing velocities for the same range of velocities shown in Fig. 15

4.2.2 Spectra

The evolution of the spectra with an increasing velocity is shown on Fig. 16 in which the arrows indicate the

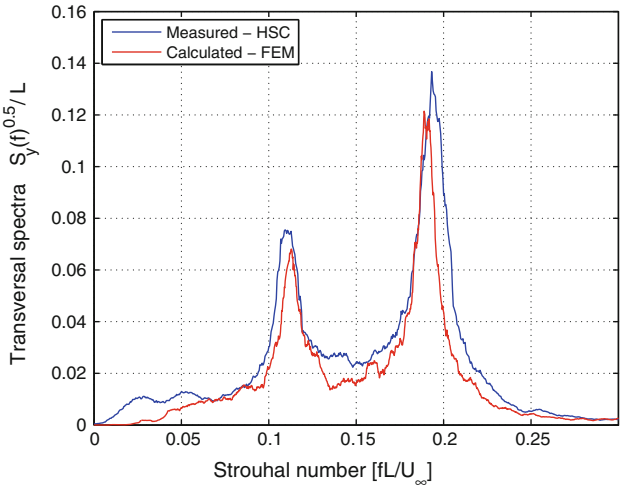

Fig. 17 Measured and calculated transversal displacement spectra example. U_∞= 24.8 m/s, Re = 169,000. See Fig. 11

tendencies of the peaks. Both longitudinal and transversal spectra present a peak at the first eigenfrequency of the flexible mode 46.5 Hz. The transversal spectra show another peak at the vortex shedding frequency; being the Strouhal number constant ($St = 0.107$), this frequency increases linearly with velocity. The resonance of the flexible model will happen when both peaks meet. The limit of the operating conditions of the wind tunnel did not allow to reaching this state. It would have not produced satisfactory results anyways since it is a coupled regime that cannot be studied with the present methodology as already discussed in Sect. 3.

Figure 17 shows the comparison of the measured and *FEM*-calculated spectra at an arbitrary reference velocity ($U_\infty = 24.5$ m/s). In the transversal direction, it can be seen that not only the statistical values of σ_y are comparable but also the dynamic characteristics of the response are well estimated by the *FEM* calculations. In the case of the longitudinal spectra, the agreement is only qualitative, since it was already discussed that the calculated response in this direction is around double of what was measured. In this case, the frequency axis is expressed in terms of Strouhal number and the vortex shedding occurs always at 0.107 as was already predicted by the unsteady pressure analysis.

5 Conclusions

The objectives of the present work are two: the development of a cost-saving measurement technique for the analysis of unsteady pressure on surfaces and the evaluation of its potential by a practical application. The selected example is the study of turbulent buffeting of a square cylinder.

The development of the measurement technique based on miniature microphones is based on the correct estimation of the response of the whole system—i.e., the microphone itself, the conditioners/amplifiers, the T-junction, the pressure line, etc. This is done with the help of an ad hoc-designed calibration tube with a small speaker at one end that is able to generate pressure fluctuations in a very wide range of frequencies.

The calibration relies on Fourier transforms of the signals and simple operations in the frequency domain. The reconstruction on the pressure at the model surface is done using an inverse Fourier transformation. The validation test shows good agreement with reference measurements; the standard deviation of the difference between reference and reconstructed pressures has always found to be less than 6.1 % of the standard deviation of the reference pressure.

This technique can be used in a wide range of applications. It allows accurate measurements of low-amplitude surface pressure fluctuations in a wide range of frequencies. This is specially interesting when the number of simultaneous measurements—and therefore sensors—is high, allowing to reduce the cost of the equipment between one and two orders of magnitude if compared with today's standards. The technique is also versatile because of two reasons: The calibration can be done in situ and the space needed on the model is very reduced, always allowing measurements whenever a pressure tap and a pressure line can be fit inside the model.

The measurement technique potential is shown in a turbulent buffeting study, the structural response of a flexible square cylinder immersed in a low-turbulence homogeneous flow: The pressure loads on a rigid model surfaces have been measured and analyzed, and they have been used as input forces for dynamic FEM calculations. High-speed imaging has been used to compare the results of the calculated displacements to those measured on a fully elastic model.

Despite the big limitations of the current setup—only 14 simultaneous surface pressure measurements—a good qualitative agreement is found between measured and calculated displacements. This agreement is also quantitative for the transversal direction of vibration in which the displacements and loads are more important.

Acknowledgments The first author has been supported with the Research Master in Fluid Dynamics scholarship of the von Karman Institute for Fluid Dynamics in Belgium.

References

Basten TGH, de Bree HA (2010) Full bandwidth calibration procedure for acoustic probes containing a pressure and particle velocity sensor. J Acoust Soc Am 127:264–270

Bergh H, Tijdeman H (1965) Theoretical and experimental results for the dynamic response of pressure measuring systems. Technical report NLR-TR F.238, National Luchten Ruimtevaartlaboratorium

Dassault Systems–Simulia: Abaqus theory manual. 3.5.1 Beam element overview

Davenport AG, Novak M (2010) Vibrations of structures induced by wind, 6th edn. McGraw-Hill, New York

Duda RO, Hart PE (1972) Use of the hough transformation to detect lines and curves in pictures. Commun ACM 15:11–15

Gumley SJ (1983) A detailed design method for pneumatic tubing systems. J Wind Eng Ind Aerodyn 13:441–452

Holmes JD (1990) Analysis and synthesis of pressure fluctuations on bluff bodies using eigenvectors. J Wind Eng Ind Aerodyn 33:219–230

Johnston RT, Sullivan JP (1994) An inexpensive pressure transducer for the measurement of low amplitude unsteady pressure signals. Exp Fluids 16:342–344

Kareem A (1990) Measurements of pressure and force fields on building models in simulated atmospheric flows. J Wind Eng Ind Aerodyn 36:589–599

Kareem A, Cermak JE (1984) Pressure fluctuations on a square building model in boundary-layer flows. J Wind Eng Ind Aerodyn 16:17–41

Kendall JM (1990) Boundary layer receptivity to freestream turbulence. AIAA paper 90-1504

Lee BE (1975) The effect of turbulence on the surface pressure field of a square prism. J Fluid Mech 69:263–282

Lee I, Sung HJ (1999) Development of an array of pressure sensors with pvdf film. Exp Fluids 26:27–35

Lee I, Sung HJ (2002) Multiple-arrayed pressure measurement for investigation of the unsteady flow structure of a reattaching shear layer. J Fluid Mech 463:377–402

Sullivan CJ, Mueller TJ (1999) Polyvinylidene fluoride film sensors for measurement of unsteady pressures on aerodynamic surfaces. Part I: design, fabrication, calibration and demonstration. Exp Fluids 27:79–84

Surry D, Djakovich D (1995) Fluctuating pressures on models of tall buildings. J Wind Eng Ind Aerodyn 58:81–112

Surry D, Stathopoulos T, Davenport AG (1983) Simple measurements techniques for area wind loads. J Eng Mech 109:1058–1071

Vickery BJ (1990) Experimental techniques for the determination of the dynamic responses of structures to wind. Meccanica 25:147–158